International Tables for Crystallography (2006). Vol. F, Chapter 19.2, pp. 423–427.

19.2. Electron diffraction of protein crystals

BY W. CHIU

19.2.1. Electron scattering

When an electron interacts with a free atom, it is simultaneously attracted to the nucleus because of the nuclear positive charge and repelled by the electrons of the atom. An electron scattering event is a composite of these forces (Hirsch *et al.*, 1977). Mathematically speaking, an electron 'sees' the potential function of the atom, which can be approximated as a 'screened Coulomb potential function'. This function is often referred to as a mass-density function and is analogous to the electron-density function in the case of an X-ray photon, which is scattered only by the electrons of an atom.

Because of the strong interactions between an electron and an atom, the scattering cross section of an atom is much higher for electrons than it is for X-rays. For a 100 keV electron, it is about 10^4 times greater than for an X-ray. For every single electron scattering event of a carbon atom, there is more than a 60% probability that the electron will lose part of its energy, which is called inelastic scattering. The energy lost is primarily in the range 10 to 20 eV, which is sufficient to induce excitation and ionization of the atoms upon irradiation (Isaacson, 1977). This energy transfer to a molecule results in breakage of chemical bonds and mass migration of broken molecular fragments.

19.2.2. The electron microscope

An electron microscope is conceptually analogous to a light microscope. It consists of an electron source, condenser lenses, an objective lens, projector lenses and a camera recorder. Because of the electronegative property of the electron, it is possible to fabricate magnetic and electrostatic lenses to focus electrons to near atomic resolution. The most critical lens in an electron microscope is the objective lens, which forms the first diffraction pattern at its focal plane and the first image at its image plane. An electron diffraction pattern is the same as an X-ray diffraction pattern, containing only the amplitude information of the structure factor, whereas an electron image contains both the amplitude and phase information of the structure factor (Unwin & Henderson, 1975).

The condenser lens is used primarily to control the beam diameter and the flux of the electrons irradiating the specimen, whereas the projector lenses are used to magnify either a diffraction pattern or an image in a broad range. The camera length in an electron microscope is adjustable, ranging from 0.2 to 2.5 m, and allows the recording of diffraction patterns with Bragg spacings from hundreds to a fraction of an ångstrom. The magnification of an image spans from a hundred to a million times. Magnification is not a limiting factor for image resolution, however, and is typically set between 40 and 80000 times for protein electron crystallography. The most important factors that affect the instrumental resolution are the coherence of the incident electron beam, the chromatic and spherical aberrations of the objective lens, the electrical stability of the electron gun and the objective lens, and the mechanical stability of the specimen stage (Chiu & Glaeser, 1977). In general, almost all modern electron microscopes are capable of resolving a lattice spacing of 2.4 Å in a thin gold crystal. The biological structure resolution in an image of a protein crystal has not reached the instrumental resolution because of many factors related to radiation damage of the specimen. Improvements in experimental and computational methods, however, have made it feasible to image protein crystals beyond 3.7 Å resolution (see below).

The range of electron energy used in an electron microscope is between 20 and 1000 keV, which corresponds to wavelengths of 0.086–0.0087 Å. Any single microscope is built and optimized for a narrow energy range because of the complex design of a highly stable electron gun. The instrument most commonly used for molecular-biology structure research operates in the range 100 to 400 keV. Choosing the most useful electron energy is based on the desired resolution and the specimen thickness. The thicker the specimen, the higher the energy that should be used in order to avoid dynamical scattering effects and to have a sufficient depth of field, so that the electron scattering data can be interpreted with a single scattering theory. Theoretically, the specimen thickness should not exceed about 700 Å if the targeted resolution is 3.5 Å with a 400 kV microscope. Beyond this specimen thickness, the phase error of the structure factors might approach 90° at that resolution. An added advantage of using higher electron energy is to reduce the chromatic aberration effect, resulting in a better-resolved image (Brink & Chiu, 1991).

There are different types of electron emitters, including tungsten filaments, LaB_6 crystals and field emission guns, all of which use different mechanisms to generate the electrons. The field emission gun produces the brightest, most monochromatic beam. The high brightness can allow the electrons to be emitted as from a point source to irradiate the specimen with a highly parallel (*i.e.* a highly spatially coherent) illumination. The benefit of high spatial coherence is the preservation of high-resolution details in the image, even though the defocus of the objective lens is set very high in order to have low-resolution feature contrast (Zhou & Chiu, 1993). Thus, a field emission source is the best choice for high-resolution data collection.

The recording medium of an electron microscope can be an image plate, a slow-scan charge-coupled-device (CCD) camera, or photographic film. Because of their broad dynamic range and high sensitivity, both the CCD camera and the image plate are best suited for recording diffraction patterns (Brink & Chiu, 1994). However, for high-resolution image recording – when the recorded area, pixel resolution, signal-to-noise ratio and the modulation transfer function characteristics must be considered – photographic film is the optimal choice (Sherman *et al.*, 1996).

19.2.3. Data collection

19.2.3.1. *Specimen preparation*

An electron microscope column is kept at a pressure of $< 10^{-6}$ Torr (1 Torr = 133.322 Pa). Because a thin protein crystal loses its crystallinity if dried in a vacuum, its hydration can be maintained by embedding it in a thin layer of vitreous ice, glucose, or other small sugar derivatives (Unwin & Henderson, 1975; Dubochet *et al.*, 1988). The effectiveness of these preservation methods is evidenced by the high-resolution diffraction orders (out to at least 3 Å) from properly embedded protein crystals (Fig. 19.2.3.1). Since the high-resolution reflections come mostly from the protein, their diffraction intensities are largely independent of the embedding medium. However, the low-resolution diffraction intensities can be affected by the embedding medium because different media have different scattering densities relative to the protein. For any new crystal, any of the embedding media mentioned above can be used for high-resolution structural studies.

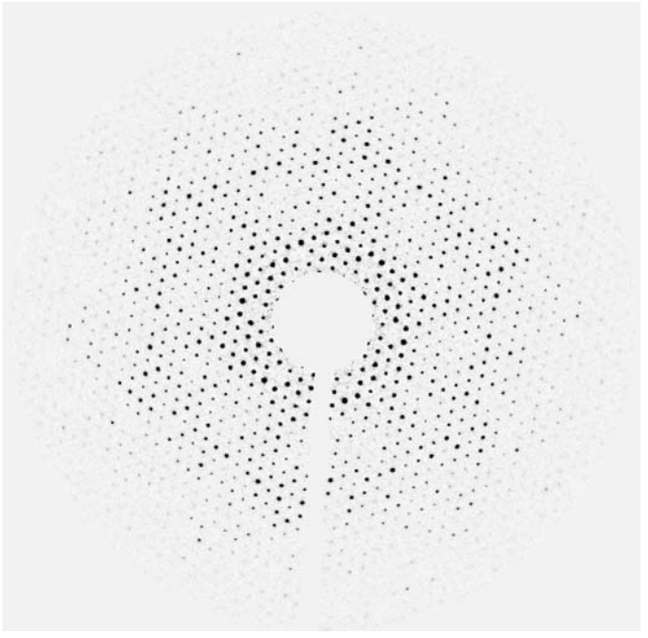

Fig. 19.2.3.1. Electron diffraction pattern of trehalose-embedded bacteriorhodopsin, with Bragg reflections extending to 2.5 Å. The unit-cell parameter of this 45 Å-thick membrane protein crystal is 62.5 × 62.5 Å arranged in a *p*3 two-dimensional space group. The raw diffraction pattern was recorded on a Gatan 2k × 2k CCD camera with 300 kV electrons in a JEOL 3000 electron cryomicroscope equipped with a field emission gun and a liquid-helium (4 K) cryoholder. The pattern displayed has been contrast-enhanced using radial background subtraction. A central beam stop was used to prevent saturation of the detector but has blocked off some reflections. R_{sym} for the Friedel-symmetry-related reflections (about 290 pairs) was computed to be about 5%. (Courtesy of Drs Yifan Cheng and Yoshinori Fujiyoshi at Kyoto University.)

19.2.3.2. *Radiation damage*

All protein crystals are prone to radiation damage caused by inelastically scattered electrons (Glaeser, 1971). This physical process is easily seen in the fading of electron diffraction intensities of a protein crystal as the accumulated doses increase. The consequence of damage is a preferential loss of the high-resolution information. Radiation damage is a dose-dependent process and cannot be reduced by adjusting the dose rate (flux) of the irradiating electrons. The strategy used to minimize the damage is to record the diffraction or image data from a specimen area that has not been previously exposed to electrons for purposes of focusing or other adjustments (Unwin & Henderson, 1975). This is called a minimal or low-dose procedure. In addition, keeping a specimen at low temperature (<113 K) allows it to tolerate a higher radiation dose (by a factor of about 4 to 6) before reaching the same extent of damage as at room temperature (Hayward & Glaeser, 1979). It has been shown that damage reduction is minimal below liquid-nitrogen temperature (Chiu *et al.*, 1981). However, there have been some impressive results using the electron cryomicroscope to study membrane protein crystals kept at liquid-helium temperature (4 K) (Kühlbrandt *et al.*, 1994; Kimura *et al.*, 1997; Miyazawa *et al.*, 1999).

19.2.3.3. *Other technical factors*

In order to record a three-dimensional data set, the crystals have to be tilted to different angles with respect to the direction of the electron beam. In a typical electron microscope, the highest angle to which the specimen stage can be tilted is about ±60°. Consequently, there is a missing set of data beyond the highest tilt angle, which corresponds to no more than 15% of the entire three-dimensional volume. Because of the radiation damage, a single diffraction pattern or a single image per crystal is usually recorded (Henderson & Unwin, 1975). The quality of a crystal is easily judged by its electron diffraction pattern as captured from a CCD camera during data collection. Evaluating the ultimate quality of images, however, takes more time and requires extensive computational analysis.

There are two major technical problems that often limit the data quality, even though a crystal is highly ordered (Henderson & Glaeser, 1985). One is the flatness of the crystal, and the other is the beam-induced movement or charging of the crystal. The effects of both problems become more prominent when the crystals are tilted to high angles. These effects tend to blur the diffraction spots, resulting in loss of high-resolution data (Brink, Sherman *et al.*, 1998). There are many ways to overcome these technical handicaps. For instance, the type of microscope grid chosen or the method of making the carbon support film is critical for reducing the wrinkling of the crystals (Butt *et al.*, 1991; Glaeser, 1992; Booy & Pawley, 1993). The use of a carbon film, which is a good conducting material, to support the protein crystal appears to reduce specimen charging (Brink, Gross *et al.*, 1998). It has been suggested that using a gold-plated objective aperture is effective in reducing specimen charging by generating a stream of secondary electrons to neutralize the positive charges that have built up on the specimen, which thus acts like an aberration-inducing electrostatic lens. Empirically, irradiating the microscope grid before depositing the specimen also reduces the charging (Miyazawa *et al.*, 1999). All these technical problems that can hamper progress in the completion of the structure determination have gradually been identified and resolved. However, more convenient and more robust experimental procedures for reducing these effects further are desirable in order to enhance the efficiency of data collection.

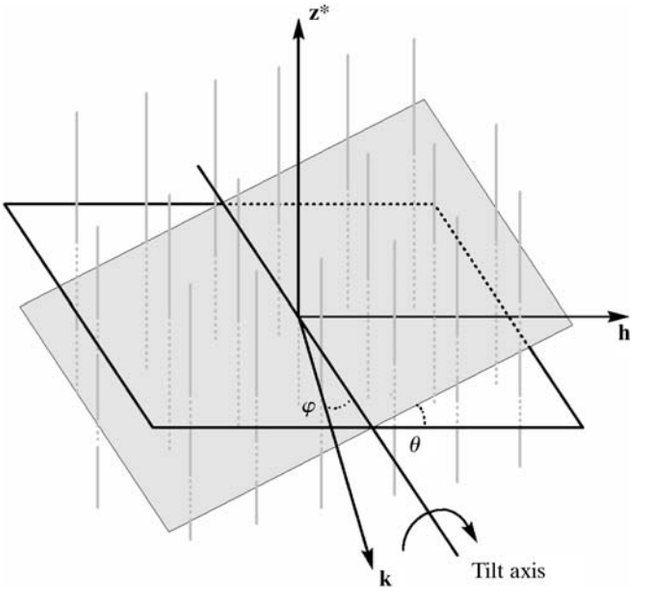

Fig. 19.2.4.1. Schematic diagram of data distribution in Fourier space for a two-dimensional crystal. Both the amplitudes and phases of the structure factors are distributed along the lattice lines passing through the (*h*, *k*) projection plane. The sectional plane shown denotes data from a crystal tilted at a certain angle (φ), and its tilt axis has an inclined angle (θ) with respect to one of its crystallographic axes. (Courtesy of Dr Jaap Brink at Baylor College of Medicine.)

19.2.4. Data processing

19.2.4.1. *Data sampling*

The principle of three-dimensional reconstruction is based on the central section theorem, which states that the experimental or computed projected diffraction pattern of a three-dimensional object is a plane that intersects the centre of the three-dimensional Fourier space in the direction normal to the direction of the projection (DeRosier & Klug, 1968). Because of the crystallographic symmetry inherent in a protein crystal, only a portion of the entire three-dimensional Fourier space, equivalent to an asymmetric unit of the crystal unit cell, is needed for the reconstruction. The structure factors of a three-dimensional crystal are localized in the three-dimensional reciprocal lattice, whereas the structure factors of a two-dimensional crystal are distributed continuously along the lattice lines, each of which passes through the reciprocal lattice in the zero projection plane (Fig. 19.2.4.1) (Henderson & Unwin, 1975). The assignment of z^* for each observation (h, k, z^*) along the lattice line is determined from the tilt angle and direction of the tilt axis for each image (Shaw & Hills, 1981). In general, the three-dimensional data set is initially built up from low-angle data and is gradually extended to the high-angle data. The angular parameters for each observed reflection are iteratively refined among one another within the whole data set. The

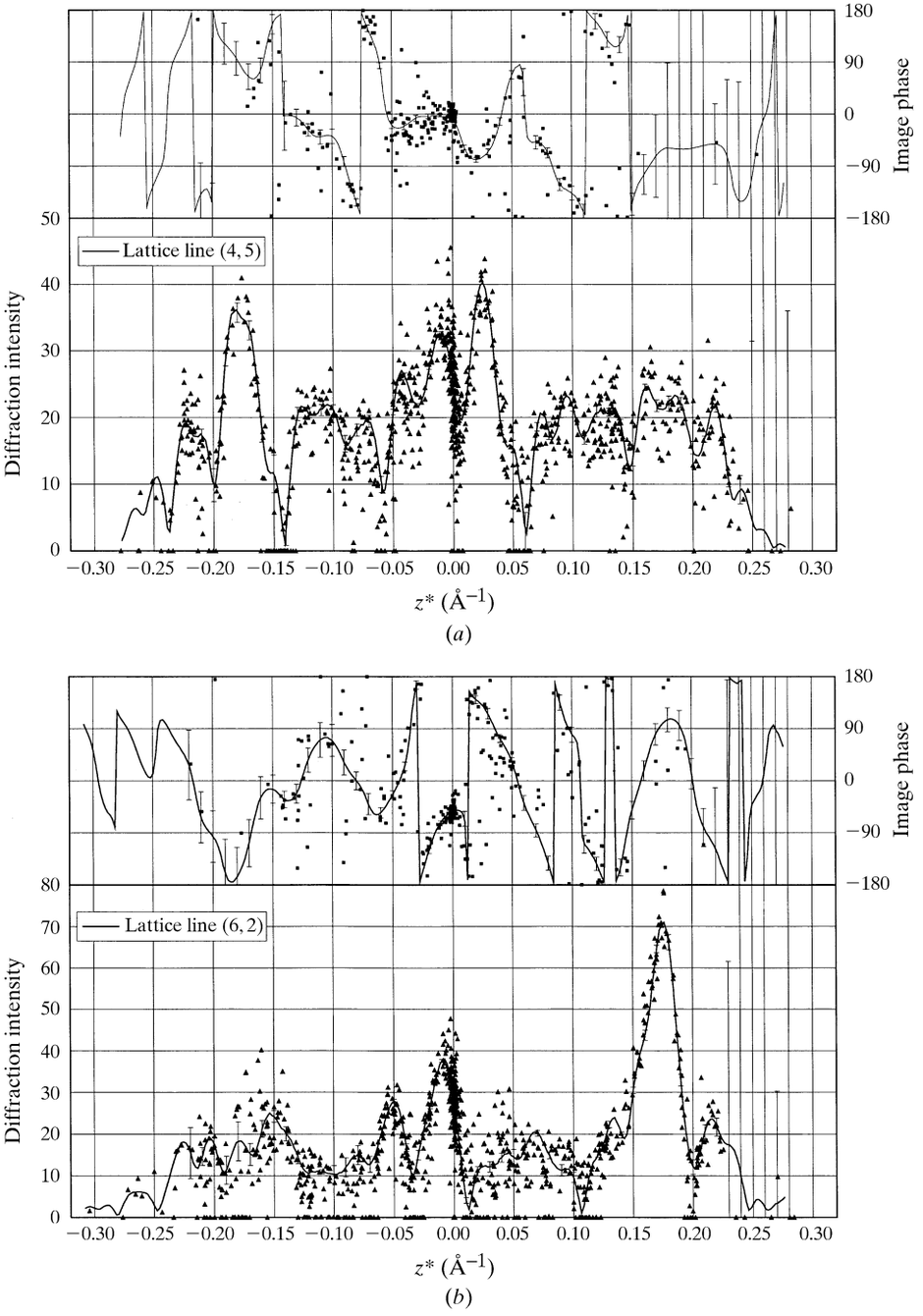

Fig. 19.2.4.2. Experimental intensities from electron diffraction patterns and phases from images of bacteriorhodopsin, recorded from tilted crystals in an electron cryomicroscope. Fitted curves for two representative lattice lines are shown: (*a*) (4, 5, z^*) and (*b*) (6, 2, z^*) (Courtesy of Drs Terushisa Hirai and Yoshinori Fujiyoshi at Kyoto University.)

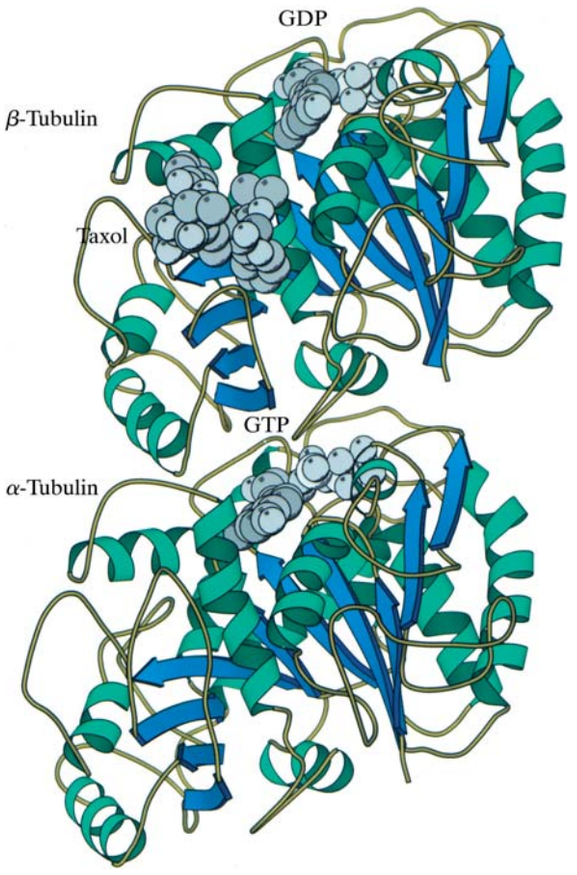

Fig. 19.2.4.3. Ribbon diagram of a tubulin dimer, whose structure has been solved to 3.7 Å resolution. GTP, GDP and taxol are shown as CPK models, with GDP at the top, bound to β tubulin, and GTP in the middle, bound to the α subunit. This is the view as seen from inside a microtubule, with the plus end at the top. (Courtesy of Drs Eva Nogales and Kenneth Downing at the Lawrence Berkeley National Laboratory, University of California, Berkeley.)

required accuracy of these angular determinations depends on the thickness of the crystal and also on the desired resolution (Prasad *et al.*, 1990). For instance, the angular accuracy has to be $< 0.1^\circ$ for 3.5 Å data in a 100 Å-thick crystal. The sampling of the data along the lattice line is generally about $\frac{1}{4}$ the thickness of the crystal (Henderson *et al.*, 1990). The data points are not evenly sampled along the lattice lines; they must be fitted into continuous and smoothly varying functions within the constraint of the crystal thickness. These functions are interpolated onto a periodic lattice, so that its inverse Fourier transform can be computed to reconstruct the three-dimensional mass-density function of the object.

19.2.4.2. *Amplitudes and phases*

An electron-microscope image contains both the amplitudes and phases of the structure factors. The basic premise of the current image-reconstruction scheme assumes that the image intensity can be related to the structure factor linearly and can be retrieved by the Fourier transform of the image intensities. However, the structure factors, $F(S)$, are influenced by several instrumental factors, as shown in equations (19.2.4.1)–(19.2.4.3) below, whose parameters need to be determined for each image.

$$F^2_{\rm obs}(S) = [F(S){\rm CTF}(S)E(S)]^2 + N^2(S), \quad (19.2.4.1)$$

$${\rm CTF}(S) = -\{(1-Q^2)^{1/2}\sin[\gamma(S)] + Q\cos[\gamma(S)]\} \text{ and} \quad (19.2.4.2)$$

$$\gamma(S) = \pi[(-C_s\lambda^3 S^4)/2 + \Delta z \lambda S^2], \quad (19.2.4.3)$$

where $F_{\rm obs}$ is the structure factor computed from the electron cryomicroscopic images, F is the true structure factor, CTF is the contrast-transfer function, E is the product of many decay functions due to the electron optics and specimen movement, N is the background noise contributed by a variety of physcial effects, S is the spatial frequency, Q is the fraction of amplitude contrast, C_s is the spherical aberration coefficient of the objective lens, λ is the wavelength and Δz is the image defocus.

In practice, it is tedious to determine all the parameters in these equations from images in order to make corrections to the amplitudes of the structure factors. In the case of crystals, the amplitudes of the structure factors can simply be obtained directly from the electron diffraction intensities, which are free from any of the above factors (Unwin & Henderson, 1975). The computational procedure used to calculate the diffraction spot intensities is similar to that used to measure an X-ray diffraction pattern (Baldwin & Henderson, 1984; Brink & Wei Tam, 1996). The quality of the diffraction intensity measurement is evaluated from the value of $R_{\rm sym}$ for Friedel-related reflections. The best data have $R_{\rm sym}$ less than 0.04. The consistency of the diffraction intensities among different patterns from different crystals is judged from $R_{\rm merge}$, which is generally 0.15–0.25 (Kimura *et al.*, 1997; Nogales *et al.*, 1998). Fig. 19.2.4.2 is an example of the diffraction intensity for two lattice lines computed from bacteriorhodopsin crystals. The phases of the structure factors are computed from images.

In addition to the instrumental factors given in equations (19.2.4.1)–(19.2.4.3), however, images are generally imperfect because of bending of the crystal, specimen preparation, or magnification variations across an image. The consequence of these imperfections is a reduction of the signal-to-noise ratio in high-resolution reflections. A computational procedure called 'unbending' has been devised, which in effect fixes the image imperfection by finding the unit-cell deviation vectors and straightening them by interpolation (Henderson *et al.*, 1986). The effect of the instrumental factors is the modulation of the phases by the oscillating function CTF(S), as shown in equations (19.2.4.1)–(19.2.4.3). The result is that the phases flip by π at different frequencies, depending on the defocus setting (Erickson & Klug, 1970). In addition, there is a phase shift caused by a combination of factors, including lens astigmatism, beam tilt and specimen height variation in a tilted position. All of these factors have to be corrected for each micrograph before merging the phases of the reflections from different micrographs to a common phase origin. The determination of the phase origin is performed by phase residual difference minimization or correlation matches among different micrographs (Amos *et al.*, 1982; Thomas & Schmid, 1995). Intensities and corresponding phases of two lattice lines are shown in Fig. 19.2.4.2. The fitted curves show the matches among the data points, each of which is from a different image or from different symmetry-related reflections from the same image.

In electron crystallography, the correctness of the phases can be evaluated by the self-consistency of the merged data sets and also by the phase residual difference of the symmetry-related reflections according to the two-dimensional plane-group symmetry. For two-dimensional crystals, there are only 17 possible plane groups (Amos *et al.*, 1982). As in the case of a three-dimensional crystal, the plane group is determined from the symmetry of the phases, the unit-cell parameters and the pattern of forbidden reflections. The plane-group assignment can be confirmed by the phase equivalence of symmetry-related reflections. Furthermore, the reliability of the

map can be judged by the figure of merit of the phases, computed from the phase probability distribution function of the observed reflections.

19.2.4.3. *3D map*

The three-dimensional (3D) map is computed from the amplitudes and phases at the resolution defined by the data (Henderson & Unwin, 1975). The resolution reported for the structure is defined by the observed reflections in the images. Owing to the missing data at high tilt angles, the reconstruction normally has a lower resolution in the direction of the electron beam than in the direction normal to it. As a result, many of the initial low-resolution structures appear stretched out along the vertical direction. The interpretation of the 3D map derived from electron crystallography is similar to that of X-ray crystallography. Often, the initial map is reported at about 7 Å, where some of the α-helices can be interpreted. With an improved map of about 3.5 Å, the polypeptide backbone is traced and some of the bulky side chains are recognized. Fig. 19.2.4.3 shows a chain tracing of a tubulin crystal (Nogales *et al.*, 1998).

19.2.4.4. *Refinement*

In order to arrive at a correct mechanistic model for the protein, an accurate atomic structure is needed. So far, in electron crystallography only bacteriorhodopsin has been refined (Grigorieff *et al.*, 1996). A common criterion used in X-ray crystallography to evaluate the progress of refinement is based on the free *R* factor, which measures the agreement between the model and a part of the experimental data not included in the refinement process. In electron crystallography, the phases are measured independently from images and hence are not refined. Therefore, they can be used as a 'free phase residual,' which is analogous to the free *R* factor, to assess the progress of refinement. The refined structure would result in improved peptide geometry, increased accuracy of the coordinates of the polypeptide backbone and of the amino-acid side chain residues, and improved temperature factors of the residues.

19.2.5. Future development

Electron crystallography has proven to be a high-resolution structural tool for two-dimensional protein crystals, to the point where the polypeptide backbone can be traced and atomic coordinates derived. Needless to say, there is still much to be learned about how to make highly ordered two-dimensional crystals from either membrane or soluble proteins. Research in this direction is critical for the growth of electron crystallography. Recent results have promoted optimism; there has been an increase in the number of membrane proteins crystallized into two-dimensional arrays from which at least 6 to 8 Å structures can be obtained (Walz *et al.*, 1997; Auer *et al.*, 1998; Zhang *et al.*, 1998; Unger *et al.*, 1999).

In the most recent high-resolution structural study of tubulin, a 3.7 Å map was obtained from 100 electron diffraction patterns and 150 electron images. Effectively, this structure was the result of a computational average of about one million tubulin dimers. It took six years to determine the structure from the time when the first high-resolution crystal structure was reported (Downing & Jontes, 1992; Nogales *et al.*, 1998). All the experimental and computational procedures were basically the same as those developed for bacteriorhodopsin (Henderson *et al.*, 1990). An obvious future development in protein electron crystallography would be aimed at improving the throughput of the structural determination. This entails a search for better solutions to some of the technical problems mentioned above as well as the introduction of automation in both data collection and processing.

Finally, another potentially exciting aspect of electron crystallography is the ability to detect charged residues from the high scattering differences between neutral and charged atoms. This physical property may make electron crystallography a unique method for detecting the ionization state of the amino-acid residues in proteins (Mitsuoka *et al.*, 1999). Furthermore, there is also a good prospect of extending the structure close to 2 Å resolution, as the next generation of electron cryomicroscope will be equipped with a field emission gun operated at 300 keV, a liquid helium cryo-specimen stage and an energy filter. This combination of instrumental features is likely to bring electron crystallography a step closer to its ultimate potential for structural biology research at the atomic level.

Acknowledgements

Research has been supported by RR002250. I thank Drs Jacob Brink, Michael Schmid, Karou Mitsuoka and Ken Downing for helpful comments on the manuscript.

(Wüthrich & Wagner, 1975) was a genuine surprise for the following reasons. In the refined X-ray crystal structure of BPTI, the aromatic rings of phenylalanine and tyrosine are among the side chains with the smallest temperature factors. For each ring, the relative values of the *B* factors increase toward the periphery, so that the largest positional uncertainty is indicated for carbon atom 4 on the symmetry axis through the C^{β}—C^{1} bond, rather than for the carbon atoms 2, 3, 5 and 6 (Fig. 19.7.5.1), which undergo extensive movements during the ring flips. Theoretical studies then showed that the crystallographic *B* factors sample multiple rotation states about the C^{α}—C^{β} bond, whereas the ring flips about the C^{β}—C^{1} bond seen by NMR are very rapid 180° rotations connecting two indistinguishable equilibrium orientations of the ring. The *B* factors do not manifest these rotational motions because the populations of all non-equilibrium rotational states about the C^{β}—C^{1} bond are vanishingly small. The ring-flip phenomenon is now a well established feature of globular proteins, manifesting ubiquitous low-frequency internal motions with activation energies of 60–100 kJ mol^{-1}, amplitudes of $\gtrsim$1.0 Å and activation volumes of about 50 $Å^3$ (Wagner, 1980), and involving concerted displacement of numerous groups of atoms (Fig. 19.7.5.1).

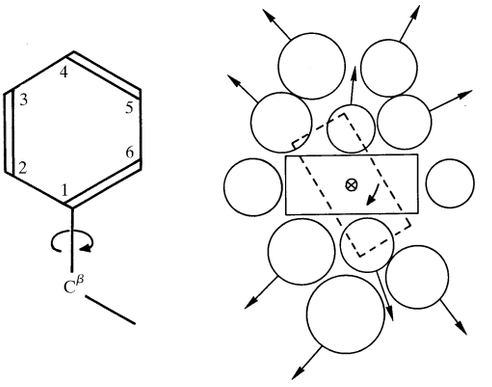

Fig. 19.7.5.1. 180° ring flips of tyrosine and phenylalanine about the C^{β}—C^{1} bond. On the left, the atom numbering is given and the χ^2 rotation axis is identified with an arrow. The drawing on the right presents a view along the C^{β}—C^{1} bond of a flipping ring in the interior of a protein, where the broken lines indicate a transient orientation of the ring plane during the flip. The circles represent atom groups near the ring, and arrows indicate movements of atom groups during the ring flip (Wüthrich, 1986).

References

19.1

Bacon, G. E. (1975). *Neutron diffraction*, pp. 155–188. Oxford: Clarendon Press.

Bentley, G. A. & Mason, S. A. (1980). *Neutron diffraction studies of proteins. Philos. Trans. R. Soc. London Ser. B*, **290**, 505–510.

Caine, J. E., Norvell, J. C. & Schoenborn, B. P. (1976). *Linear position-sensitive counter system for protein crystallography. Brookhaven Symp. Biol.* **27**, 43–50.

Hanson, J. C. & Schoenborn, B. P. (1981). *Real space refinement of neutron diffraction data from sperm whale carbonmonoxymyoglobin. J. Mol. Biol.* **153**, 117–146.

Kossiakoff, A. A. (1983). *Neutron protein crystallography: advances in methods and applications. Annu. Rev. Biophys. Bioeng.* **12**, 259–282.

Kossiakoff, A. A. (1985). *The application of neutron crystallography to the study of dynamic and hydration properties of proteins. Annu. Rev. Biochem.* **54**, 1195–1227.

Kossiakoff, A. A., Shpungin, J. & Sintchak, M. D. (1990). *Hydroxyl hydrogen conformations in trypsin determined by the neutron solvent difference map method: relative importance of steric and electrostatic factors in defining hydrogen-bonding geometries. Proc. Natl Acad. Sci. USA*, **87**, 4468–4472.

Kossiakoff, A. A. & Shteyn, S. (1984). *Effect of protein packing structure on side-chain methyl rotor conformations. Nature (London)*, **311**, 582–583.

Kossiakoff, A. A., Sintchak, M. D., Shpungin, J. & Presta, L. G. (1992). *Analysis of solvent structure in proteins using neutron $D_2O - H_2O$ solvent maps: pattern of primary and secondary hydration of trypsin. Proteins Struct. Funct. Genet.* **12**, 223–236.

Kossiakoff, A. A. & Spencer, S. A. (1980). *Neutron diffraction identifies His 57 as the catalytic base in trypsin. Nature (London)*, **288**, 414–416.

Kossiakoff, A. A. & Spencer, S. A. (1981). *Direct determination of the protonation states of aspartic acid-102 and histidine-57 in the tetrahedral intermediate of the serine proteases: neutron structure of trypsin. Biochemistry*, **20**, 6462–6474.

McDowell, R. S. & Kossiakoff, A. A. (1995). *A comparison of neutron diffraction and molecular dynamics structures: hydroxyl group and water molecular orientations in trypsin. J. Mol. Biol.* **250**, 553–570.

Niimura, N., Minezaki, Y., Nonaka, T., Castagna, J.-C., Cipriani, F., Hoghoj, P., Lehmann, M. S. & Wilkinson, C. (1997). *Neutron Laue diffractometry with an imaging plate provides an effective data collection regime for neutron protein crystallography. Nature Struct. Biol.* **4**, 909–914.

Norvell, J. C. & Schoenborn, B. P. (1976). *Use of the tangent formula for the refinement of neutron protein data. Brookhaven Symp. Biol.* **27**, 1124–1130.

Phillips, S. E. V. (1984). *Hydrogen bonding and exchange in oxymyoglobin*. In *Neutrons in biology*, edited by B. P. Schoenborn, pp. 305–322. New York: Plenum Press.

Prince, E., Wlodawer, A. & Santoro, A. (1978). *Flat-cone diffractometer utilizing a linear position-sensitive detector. J. Appl. Cryst.* **11**, 173–178.

Schoenborn, B. P. (1975). *Anomalous scattering*. In *Conference on anomalous scattering*, edited by S. Rameseshan & S. C. Abrahams, pp. 407–421. Copenhagen: Munksgaard.

Schoenborn, B. P. & Diamond, R. (1976). *Neutron diffraction analysis of metmyoglobin. Brookhaven Symp. Biol.* **27**, 3–11.

Shpungin, J. & Kossiakoff, A. A. (1986). *A method of solvent structure analysis for proteins using $D_2O - H_2O$ neutron difference maps. Methods Enzymol.* **127**, 329–342.

Teeter, M. M. & Kossiakoff, A. A. (1984). *The neutron structure of the hydrophobic plant protein crambin*. In *Neutrons in biology*, edited by B. P. Schoenborn, pp. 335–348. New York: Plenum Press.

Wilkinson, C., Gabriel, A., Lehmann, M. S., Zemb, T. & Ne, F. (1992). *Image plate neutron detector. Proc. Soc. Photo-Opt. Instrum. Eng.* **1737**, 324–329.

Wilkinson, C. & Lehmann, M. S. (1991). *Quasi-Laue neturon diffractometer*. *Nucl. Instrum. Methods A*, **310**, 411–415.

Wlodawer, A. & Hendrickson, W. A. (1982). *A procedure for joint refinement of macromolecular structures with X-ray and neutron diffraction data from single crystals. Acta Cryst.* A**38**, 239–247.

Wlodawer, A. & Sjolin, L. (1981). *Orientation of histidine residues in RNase A: neutron diffraction study. Proc. Natl Acad. Sci. USA*, **78**, 2853–2855.

19.2

Amos, L. A., Henderson, R. & Unwin, P. N. (1982). *Three-dimensional structure determination by electron microscopy of two-dimensional crystals*. *Prog. Biophys. Mol. Biol.* **39**, 183–231.

19.2 (*cont.*)

Auer, M., Scarborough, G. A. & Kühlbrandt, W. (1998). *Three-dimensional map of the plasma membrane H^+-ATPase in the open conformation*. *Nature (London)*, **392**, 840–843.

Baldwin, J. & Henderson, R. (1984). *Measurement and evaluation of electron diffraction patterns from two-dimensional crystals*. *Ultramicroscopy*, **14**, 319–336.

Booy, F. P. & Pawley, J. B. (1993). *Cryo-crinkling: what happens to carbon films on copper grids at low temperature*. *Ultramicroscopy*, **48**, 273–280.

Brink, J. & Chiu, W. (1991). *Contrast analysis of cryo-images of n-paraffin recorded at 400 kV out to 2.1 Å resolution*. *J. Microsc.* **161**, 279–295.

Brink, J. & Chiu, W. (1994). *Applications of a slow-scan CCD camera in protein electron crystallography*. *J. Struct. Biol.* **113**, 23–34.

Brink, J., Gross, H., Tittmann, P., Sherman, M. B. & Chiu, W. (1998). *Reduction of charging in protein electron cryomicroscopy*. *J. Microsc.* **191**, 67–73.

Brink, J., Sherman, M. B., Berriman, J. & Chiu, W. (1998). *Evaluation of charging on macromolecules in electron cryomicroscopy*. *Ultramicroscopy*, **72**, 41–52.

Brink, J. & Wei Tam, M. (1996). *Processing of electron diffraction patterns acquired on a slow-scan CCD camera*. *J. Struct. Biol.* **116**, 144–149.

Butt, H. J., Wang, D. N., Hansma, P. K. & Kühlbrandt, W. (1991). *Effect of surface roughness of carbon support films on high-resolution electron diffraction of two-dimensional protein crystals*. *Ultramicroscopy*, **36**, 307–318.

Chiu, W. & Glaeser, R. M. (1977). *Factors affecting high resolution fixed-beam transmission electron microscopy*. *Ultramicroscopy*, **2**, 207–217.

Chiu, W., Knapek, E., Jeng, T. W. & Dietrick, I. (1981). *Electron radiation damage of a thin protein crystal at 4 K*. *Ultramicroscopy*, **6**, 291–296.

DeRosier, D. J. & Klug, A. (1968). *Reconstruction of three-dimensional structures from electron micrographs*. *Nature (London)*, **217**, 130–134.

Downing, K. H. & Jontes, J. (1992). *Projection map of tubulin in zinc-induced sheets at 4 Å resolution*. *J. Struct. Biol.* **109**, 152–159.

Dubochet, J., Adrian, M., Chang, J.-J., Homo, J.-C., Lepault, J., McDowall, A. W. & Schultz, P. (1988). *Cryo-electron microscopy of vitrified specimens*. *Q. Rev. Biophys.* **21**, 129–228.

Erickson, H. P. & Klug, A. (1970). *The Fourier transform of an electron micrograph: effects of defocusing and aberrations, and implications for the use of underfocus contrast enhancement*. *Philos. Trans. R. Soc. London Ser. B*, **261**, 105–118.

Glaeser, R. M. (1971). *Limitations to significant information in biological electron microscopy as a result of radiation damage*. *J. Ultrastruct. Res.* **36**, 466–482.

Glaeser, R. M. (1992). *Specimen flatness of thin crystalline arrays: influence of the substrate*. *Ultramicroscopy*, **46**, 33–43.

Grigorieff, N., Ceska, T. A., Downing, K. H., Baldwin, J. M. & Henderson, R. (1996). *Electron-crystallographic refinement of the structure of bacteriorhodopsin*. *J. Mol. Biol.* **259**, 393–421.

Hayward, S. B. & Glaeser, R. M. (1979). *Radiation damage of purple membrane at low temperature*. *Ultramicroscopy*, **4**, 201–210.

Henderson, R., Baldwin, J. M., Ceska, T. A., Zemlin, F., Beckmann, E. & Downing, K. H. (1990). *Model for the structure of bacteriorhodopsin based on high-resolution electron cryo-microscopy*. *J. Mol. Biol.* **213**, 899–929.

Henderson, R., Baldwin, J. M., Downing, K. H., Lepault, J. & Zemlin, F. (1986). *Structure of purple membrane from Halobacterium halobium: recording, measurement and evaluation of electron micrographs at 3.5 Å resolution*. *Ultramicroscopy*, **19**, 147–178.

Henderson, R. & Glaeser, R. M. (1985). *Quantitative analysis of image contrast in electron micrographs of beam-sensitive crystals*. *Ultramicroscopy*, **16**, 139–150.

Henderson, R. & Unwin, P. N. (1975). *Three-dimensional model of purple membrane obtained by electron microscopy*. *Nature (London)*, **257**, 28–32.

Hirsch, P., Howie, A., Nicholson, R. B., Pashley, D. W. & Whelan, M. J. (1977). *Electron microscopy of thin crystals*. Huntington: Robert K. Krieger Publishing Co.

Isaacson, M. S. (1977). *Specimen damage in the electron microscope*. In *Principles and techniques of electron micrsocopy. Biological applications*, edited by M. A. Hyatt, pp. 1–78. New York: Van Nostrand Reinhold Co.

Kimura, Y., Vassylyev, D. G., Miyazawa, A., Kidera, A., Matsushima, M., Mitsuoka, K., Murata, K., Hirai, T. & Fujiyoshi, Y. (1997). *Surface of bacteriorhodopsin revealed by high-resolution electron crystallography*. *Nature (London)*, **389**, 206–211.

Kühlbrandt, W., Wang, D. N. & Fujiyoshi, Y. (1994). *Atomic model of plant light-harvesting complex by electron crystallography*. *Nature (London)*, **367**, 614–621.

Mitsuoka, K., Hirai, T., Murata, K., Miyazawa, A., Kidera, A., Kimura, Y. & Fujiyoshi, Y. (1999). *The structure of bacteriorhodopsin at 3.0 Å resolution based on electron crystallography: implication of the charge distribution*. *J. Mol. Biol.* **286**, 861–882.

Miyazawa, A., Fujiyoshi, Y., Stowell, M. & Unwin, N. (1999). *Nicotinic acetylcholine receptor at 4.6 Å resolution: transverse tunnels in the channel wall*. *J. Mol. Biol.* **288**, 765–786.

Nogales, E., Wolf, S. G. & Downing, K. H. (1998). *Structure of the alpha beta tubulin dimer by electron crystallography*. *Nature (London)*, **391**, 199–203.

Prasad, B. V., Degn, L. L., Jeng, T. W. & Chiu, W. (1990). *Estimation of allowable errors for tilt parameter determination in protein electron crystallography*. *Ultramicroscopy*, **33**, 281–285.

Shaw, P. J. & Hills, G. J. (1981). *Tilted specimen in the electron microscope: a simple specimen holder and the calculation of tilt angles for crystalline specimens*. *Micron*, **12**, 279–282.

Sherman, M. B., Brink, J. & Chiu, W. (1996). *Performance of a slow-scan CCD camera for macromolecular imaging in a 400 kV electron cryomicroscope*. *Micron*, **27**, 129–139.

Thomas, I. M. & Schmid, M. F. (1995). *A cross-correlation method for merging electron crystallographic image data*. *J. Micros. Soc. Am.* **1**, 167–173.

Unger, V. M., Kumar, N. M., Gilula, N. B. & Yeager, M. (1999). *Three-dimensional structure of a recombinant gap junction membrane channel*. *Science*, **283**, 1176–1180.

Unwin, P. N. & Henderson, R. (1975). *Molecular structure determination by electron microscopy of unstained crystalline specimens*. *J. Mol. Biol.* **94**, 425–440.

Walz, T., Hirai, T., Murata, K., Heymann, J. B., Mitsuoka, K., Fujiyoshi, Y., Smith, B. L., Agre, P. & Engel, A. (1997). *The three-dimensional structure of aquaporin-1*. *Nature (London)*, **387**, 624–627.

Zhang, P., Toyoshima, C., Yonekura, K., Green, N. M. & Stokes, D. L. (1998). *Structure of the calcium pump from sarcoplasmic reticulum at 8-Å resolution*. *Nature (London)*, **392**, 835–839.

Zhou, Z. H. & Chiu, W. (1993). *Prospects for using an IVEM with a FEG for imaging macromolecules towards atomic resolution*. *Ultramicroscopy*, **49**, 407–416.

19.3

Arai, M., Ikura, T., Semisotnov, G. V., Kihara, H., Amemiya, Y. & Kuwajima, K. (1998). *Kinetic refolding of β-lactoglobulin. Studies by synchrotron X-ray scattering, and circular dichroism, absorption and fluorescence spectroscopy*. *J. Mol. Biol.* **275**, 149–162.

Bonneté, F., Malfois, M., Finet, S., Tardieu, A., Lafont, S. & Veesler, S. (1997). *Different tools to study interaction potentials in γ-crystallin solutions: relevance to crystal growth*. *Acta Cryst.* D**53**, 438–447.

Boulin, C. J., Kempf, A., Gabriel, A. & Koch, M. H. J. (1988). *Data acquisition systems for linear and area X-ray detectors using delay line readout*. *Nucl. Instrum. Methods Phys. Res. A*, **269**, 312–320.